Modal separation, mapping and inverting three-component VSP data

Stéphane Labonté and Robert R. Stewart

ABSTRACT

In offset vertical seismic profiling (VSP), the large variation in angles of incidence at the geophone's location and the presence of considerable amounts of compressional (P) and shear (S) waves in the propagating wavefield requires the use of three-component geophones for full wavefield understanding. In this study, the vertical and horizontal components are used to recover the full amplitudes of P and SV waves, map the P and SV waves to their respective reflection points, and perform a reflectivity inversion on the converted wave map in an attempt to recover shear-wave velocity information.

Algorithms are derived and applied to two different data sets; a synthetic data set and a field three-component data set from the Rolling Hills area of Southern Alberta, Canada. First the data are prepared for the separation process by applying a series of processes including rotation of horizontal components, trace equalization, downgoing wavefield removal, deconvolution and time-variant gain.

For the separation of P and S waves, filter coefficients are derived by considering the particle displacement of downgoing P and SV waves at the geophone's location. The separation process requires an estimate of P and S velocities along the borehole and uses several other simplifying assumptions. The filter coefficients are not all stable for vertical slownesses larger than $1/V_S$ and are tapered to zero by a cosine function to account for this instability. The filtering process is attempted in the f - k and localized p - t domains, and the results obtained through each method are compared. It is found that the results obtained through the p - t decomposition method do not contain the 'ringing' and the smearing of the wavelet in time and in depth that result when the f - k transform is used as a mean of slowness decomposition.

The total P- and SV-wave sections are then used to map the upgoing wavefields to their respective reflection points. The results show that the mapping algorithms map the P or SV reflections within 7% of their correct offset locations and within 4% of their correct time position. The SV-wave map is used to test a velocity inversion algorithm that attempts to recover the S-wave velocities from the mapped traces. The inversion is found to give results that are within 1% of the actual velocities for the synthetic data case. For the real VSP data case, however, the inversion must be given constraints to perform adequately. The wavelet effect, caused by input data that is not spiked appropriately, is present in the inversion results of both the synthetic and the real data sets.

The need for three-component recording in VSP

Figure 1 shows a cross-sectional view of an offset VSP ray geometry. Although this scenario is made rather simple by assuming the source energy to be entirely of the P-wave type, one can see that the propagating wavefield can become rather complex. Downgoing P waves convert to downgoing S waves at geological interfaces. Furthermore, P-SV conversion occurs at the reflection point (Aki and Richards, 1980) generating an arrival time at the geophone's location that is composed of P-wave traveltime to the reflector (downgoing mode) and S-wave traveltime from the reflector to the geophone (upgoing mode).

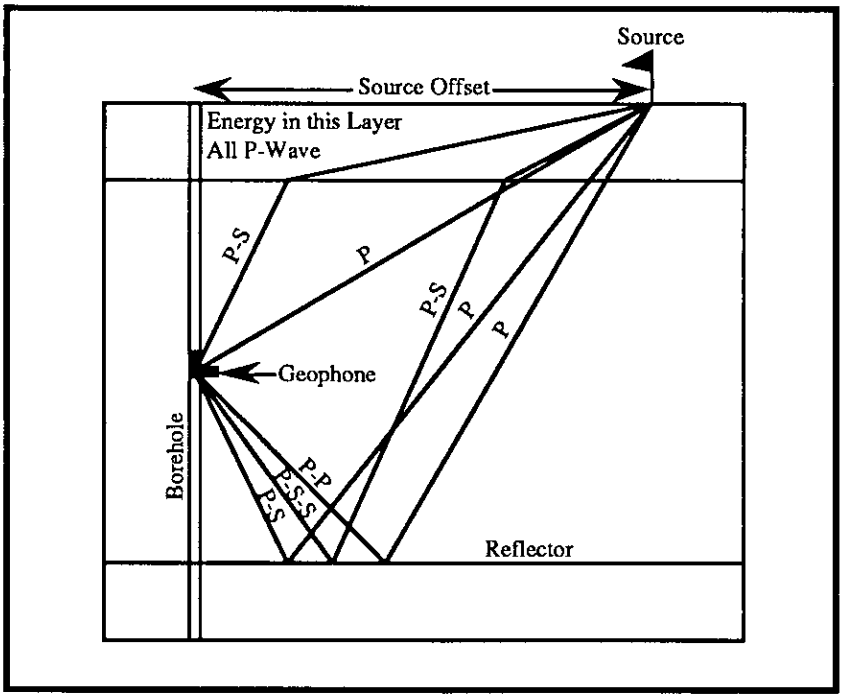

Figure 1. Offset VSP geometry.

Also shown in Figure 1 is the variation in angles of incidence for downgoing and upgoing P and S waves. At shallow receiver depths, the angle of incidence of a downgoing P or S wave is closer to the horizontal than when the geophone is located deeper in the hole where its angle of incidence is closer to the vertical. A similar argument can be followed for an upgoing P or S wave at the receiver: at shallow receiver depths for a given reflector, a reflected wave has an angle of incidence closer to the vertical than at deeper depths where its angle of incidence is further away from the vertical. Because of the variation in angles of incidence of the downgoing and upgoing wavefields, P waves are partially on the horizontal channel and part of this signal would not be recorded without a horizontal geophone. Similarly, shear waves are on the vertical geophone and cannot be unambiguously separated without other components. In order to record the full wavefield, a vertical and radial geophone (in line with the source-receiver direction) are needed to record the vertical and radial components of the propagating wavefield. By doing so, the P-wave section can be improved over the conventional method of vertical component recording, and an attempt can be made at reconstructing the S wavefield.

Synthetic and field data

The synthetic data set was generated using the Uniseis ray tracing program on the Landmark Workstation made available to the CREWES Project at the University of Calgary. The model used in the ray tracing is made of three layers overlying a half space with P- and S-wave velocities (V_P and V_S) as shown in Figure 2. The density was kept constant at 2200 kg/m^3. Both vertical and radial components were generated using the following parameters:

Number of traces (depth levels): 75
Geophone depths: 500 - 1980 m
Geophone spacing: 20 m
Source offset: 1200 m
Sample rate: 0.002 s
Wavelet: Zero phase Ricker (30 Hz).

A P-wave source was used with both P-P and P-SV reflections being generated at each interface. Downgoing mode conversion and multiples, which are often smaller in amplitude (Dillon and Thompson, 1984) were not generated in the ray tracing so that the resulting calculated wavefield would consist of a downgoing P wave and upgoing P-P and P-SV reflections. The vertical and radial components generated by the ray tracer are shown in Figures 3 and 4 with the first P breaks muted. Three P-wave (PP1, PP2, PP3) and three converted S-wave (PS1, PS2, PS3) reflection events corresponding to the three geological interfaces of the model can clearly be seen on both the vertical and the radial components.

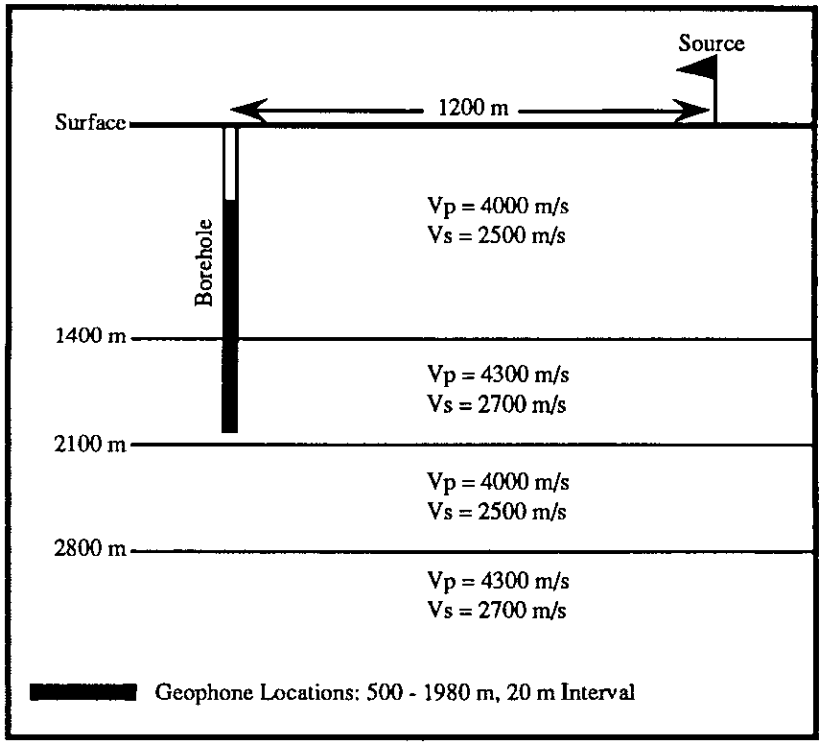

Figure 2. Synthetic model.

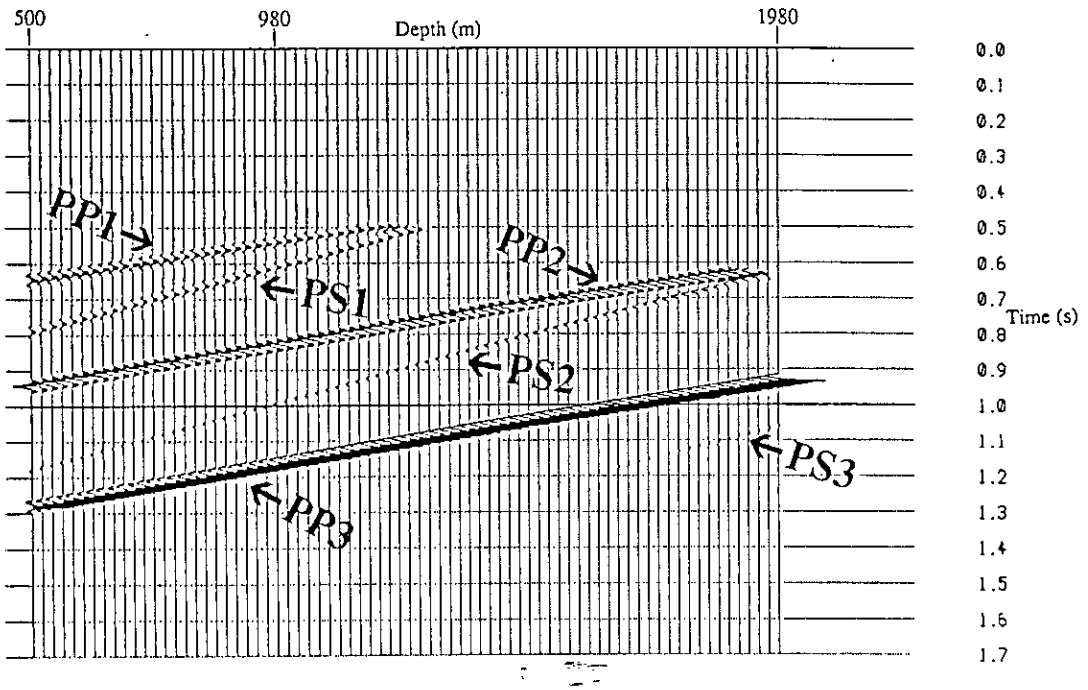

Figure 3. Vertical component of synthetic data set with first breaks muted.

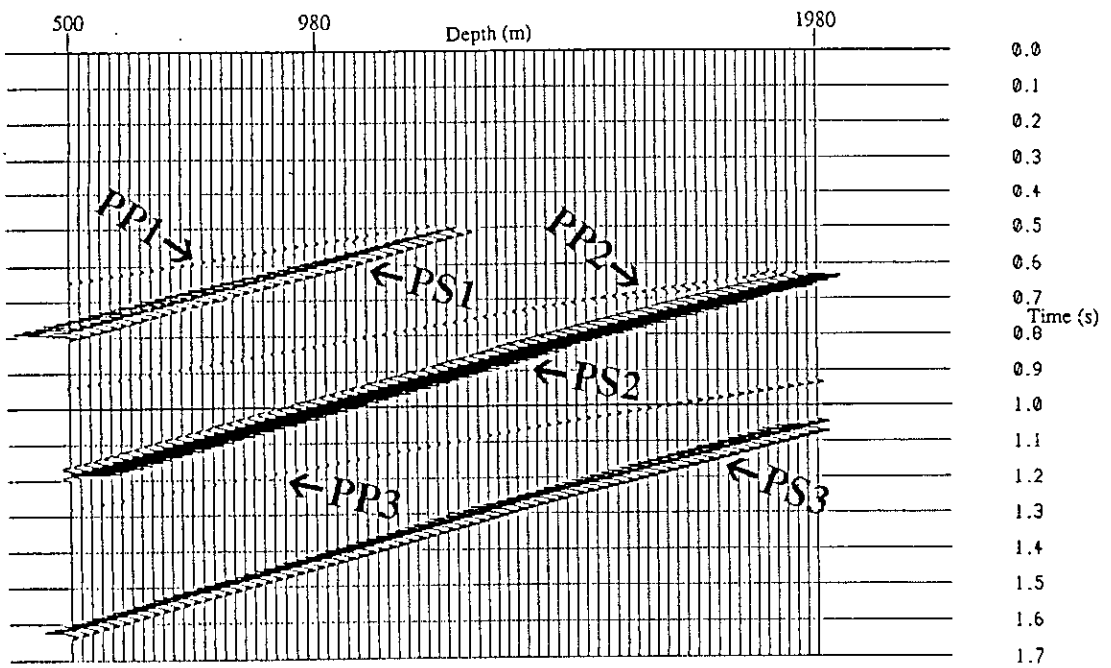

Figure 4. Radial component of synthetic data set with first breaks muted.

The real three-component data set was recorded in the fall of 1987 by Pan Canadian Petroleum Ltd. with the following parameters:

Number of traces (depth levels): 67
Geophone depths: 520 - 1840 m
Geophone spacing: 20 m
Source: P-wave vibrator (Mertz Model-16)
Sweep: 8 - 100 Hertz
Source offset: 325 m
Sample rate: 0.002 s.

The wavefield generated by the vibrator was recorded using three-component geophones. Figures 5 and 6 show the vertical and radial components of the field VSP after rotation of horizontal components, trace equalization, downgoing wavefield removal, deconvolution and time-variant gain.

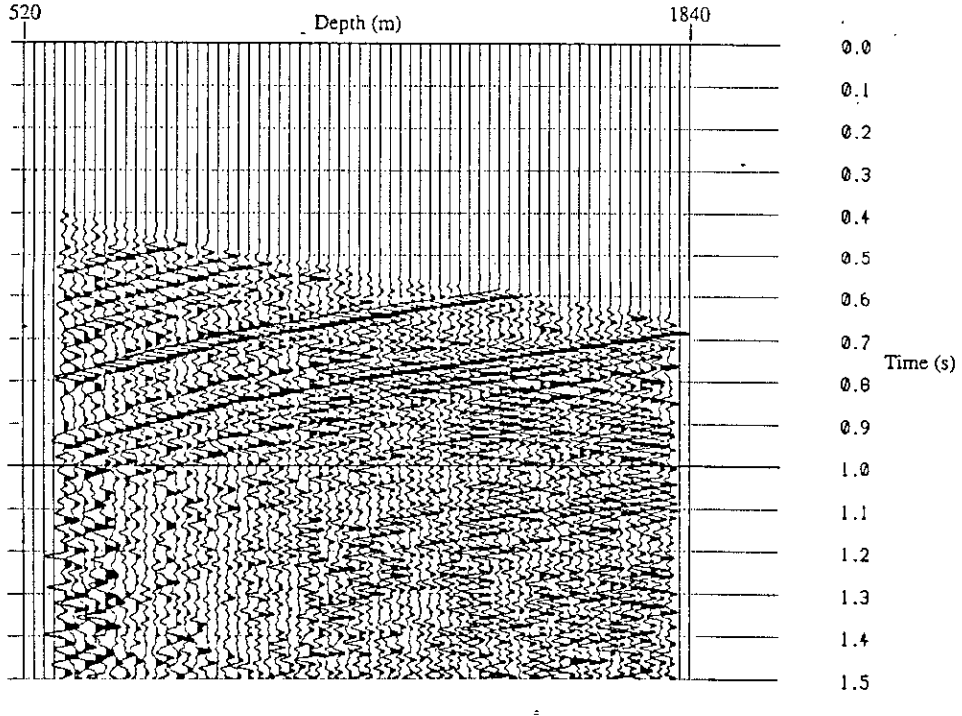

Figure 5. Deconvolved vertical component of the upgoing wavefield for the Rolling Hills data set with time-variant gain applied.

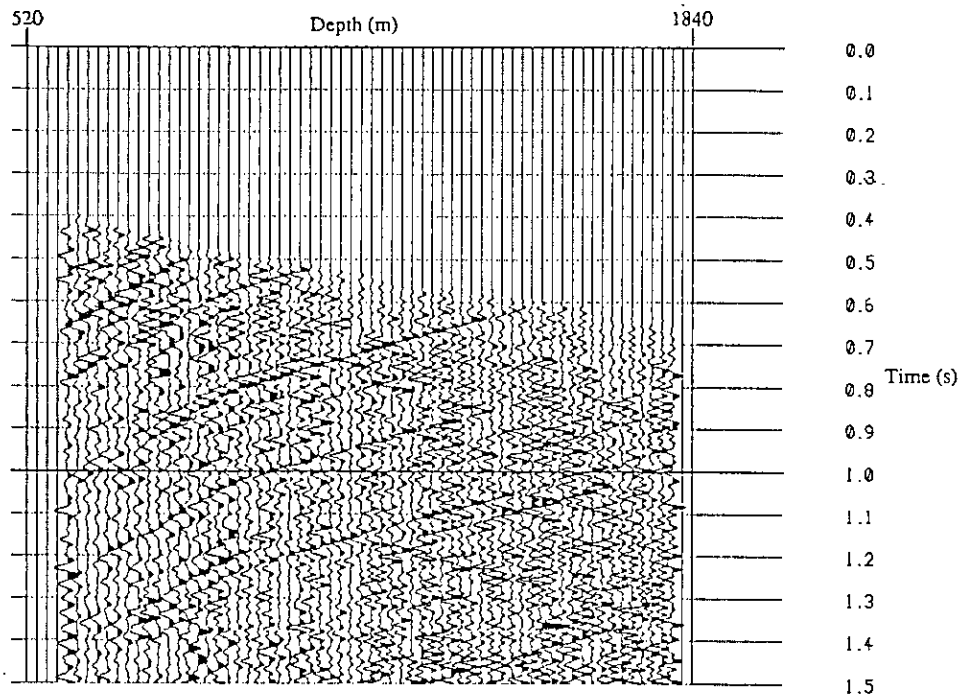

Figure 6. Deconvolved radial component of the upgoing wavefield for the Rolling Hills data set with time-variant gain applied.

P-S wave mode separation

Figure 7 shows the particle displacement of an incident P or S wave as a function of angle of incidence (after Dankbaar, 1987). From this diagram, the total displacement on the vertical ($U_z(t)$) and radial ($U_x(t)$) channels are

$$\begin{aligned} U_z(t) &= U^P(t) \sin \theta_P(t) + U^S(t) \cos \theta_S(t), \\ U_x(t) &= -U^P(t) \cos \theta_P(t) + U^S(t) \sin \theta_S(t), \end{aligned} \tag{1}$$

where $U^P(t)$ and $U^S(t)$ are the P and SV wavefields respectively. These equations can be solved for $U^P(t)$ and $U^S(t)$ yielding

$$\begin{aligned} U^P(t) &= \frac{U_z(t) \sin \theta_S(t) - U_x(t) \cos \theta_S(t)}{\sin \theta_P(t) \sin \theta_S(t) + \cos \theta_P(t) \cos \theta_S(t)}, \\ U^S(t) &= \frac{U_z(t) \cos \theta_P(t) + U_x(t) \sin \theta_P(t)}{\sin \theta_P(t) \sin \theta_S(t) + \cos \theta_P(t) \cos \theta_S(t)}. \end{aligned} \tag{2}$$

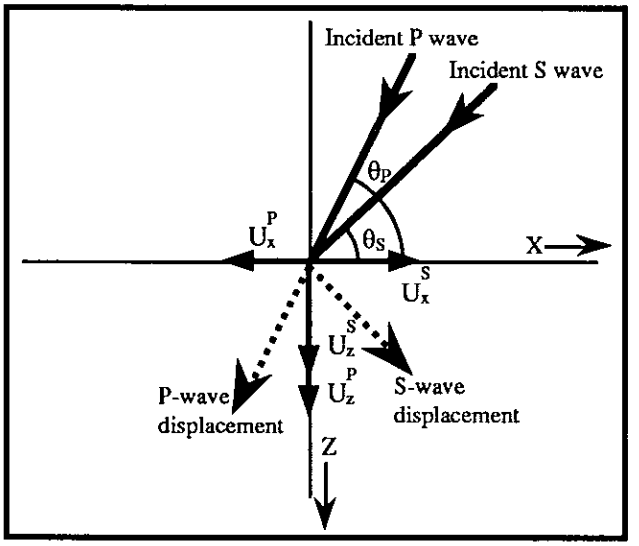

Figure 7. Particle displacement of an incident P or S wave.

Equation (2) could be used to separate P and SV waves in the depth-time domain but this would involve calculating the angle of incidence of P and SV waves at each time point on the VSP traces. Instead, the plane-wave decomposition approach is used. It can be shown that the slowness equivalent of equation (2) is

$$U^P = U_Z\left(\frac{p\,V_S}{Q}\right) + U_X\left(-\frac{\sqrt{1-(p\,V_S)^2}}{Q}\right),$$

$$U^S = U_Z\left(\frac{\sqrt{1-(p\,V_P)^2}}{Q}\right) + U_X\left(\frac{p\,V_P}{Q}\right), \qquad (3)$$

$$\text{where } Q = (p\,V_P)(p\,V_S) + \sqrt{1-(p\,V_P)^2}\,\sqrt{1-(p\,V_S)^2}.$$

Equation (3) gives the separated P and S waves as a function of the vertical and radial components (U_Z and U_X), the vertical slowness (p), and the P- and S-wave velocities (V_P and V_S). Equation (3) is equivalent to equations (2) when the filtering process is applied in the slowness domain, that is, when the vertical and radial components have previously been submitted to a plane-wave decomposition algorithm such as the two-dimensional Fourier transform or the tau-p transform; the results obtained through each of these two methods are discussed by Dankbaar (1987) and Foster and Gaiser (1986) respectively.

In this paper, the P-S separation is applied using a localized p - t decomposition approach (Cheadle, 1988). The results are shown in Figures 8 (pass P) and 9 (pass S). for the synthetic case and in Figures 10 (pass P) and 11 (pass S) for the field VSP.

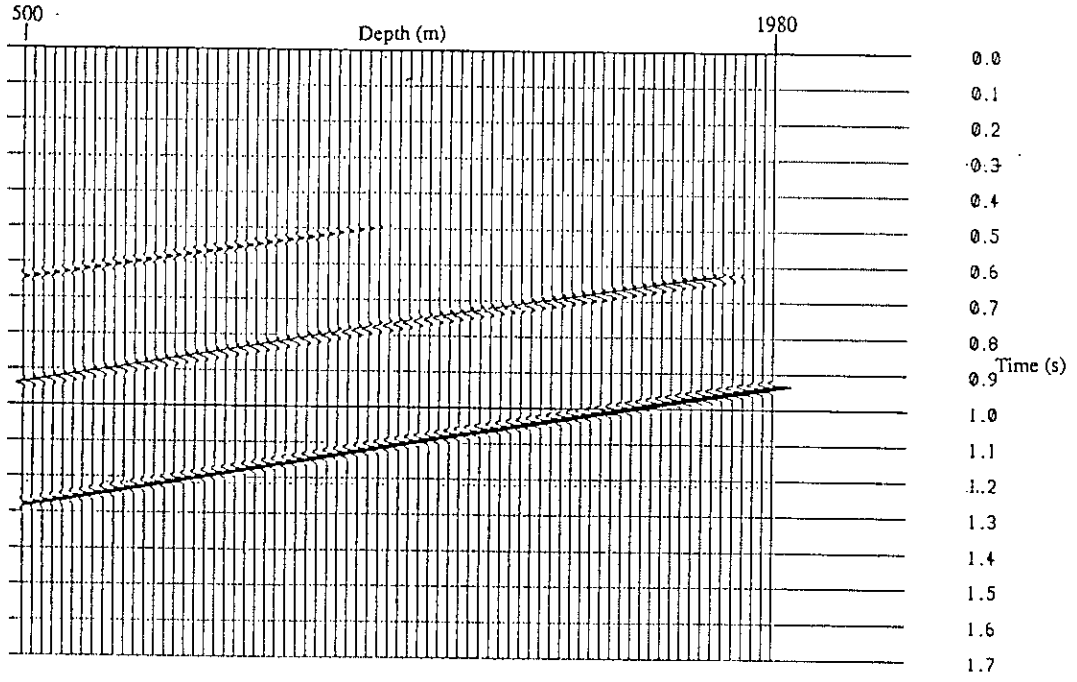

Figure 8. Pass P wavefield for the synthetic data set.

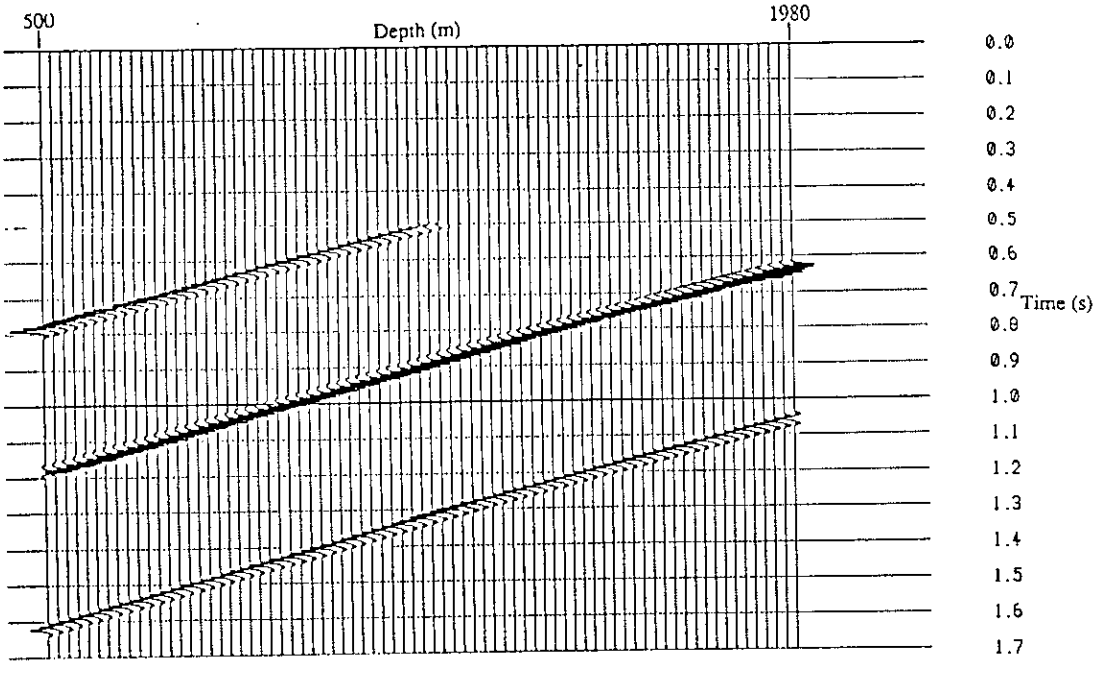

Figure 9. Pass S wavefield for the synthetic data set.

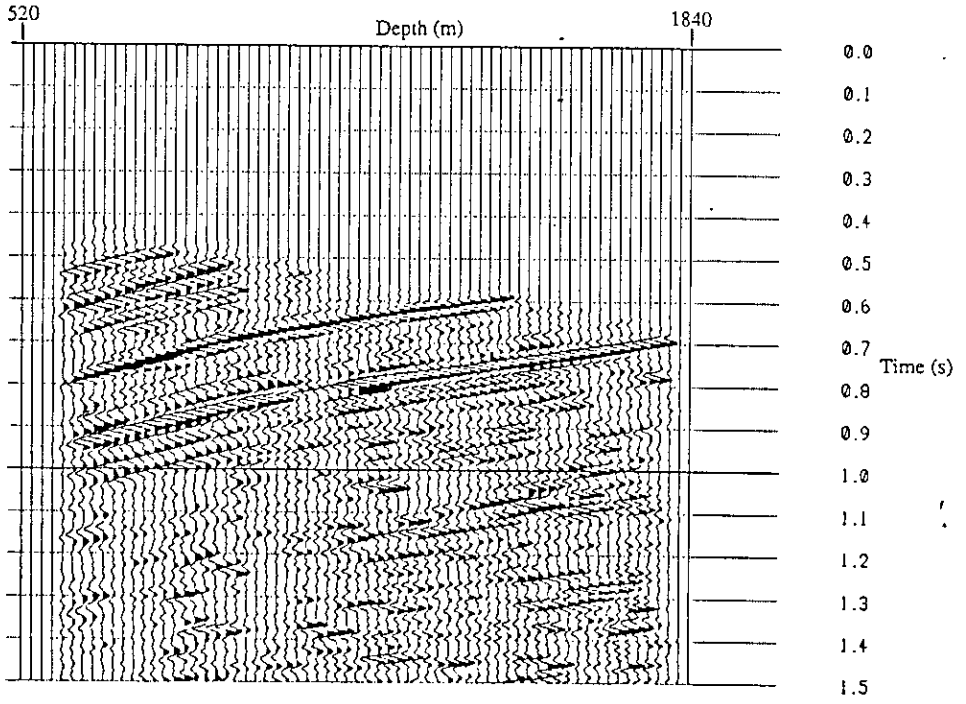

Figure 10. Pass P wavefield for the Rolling Hills data set.

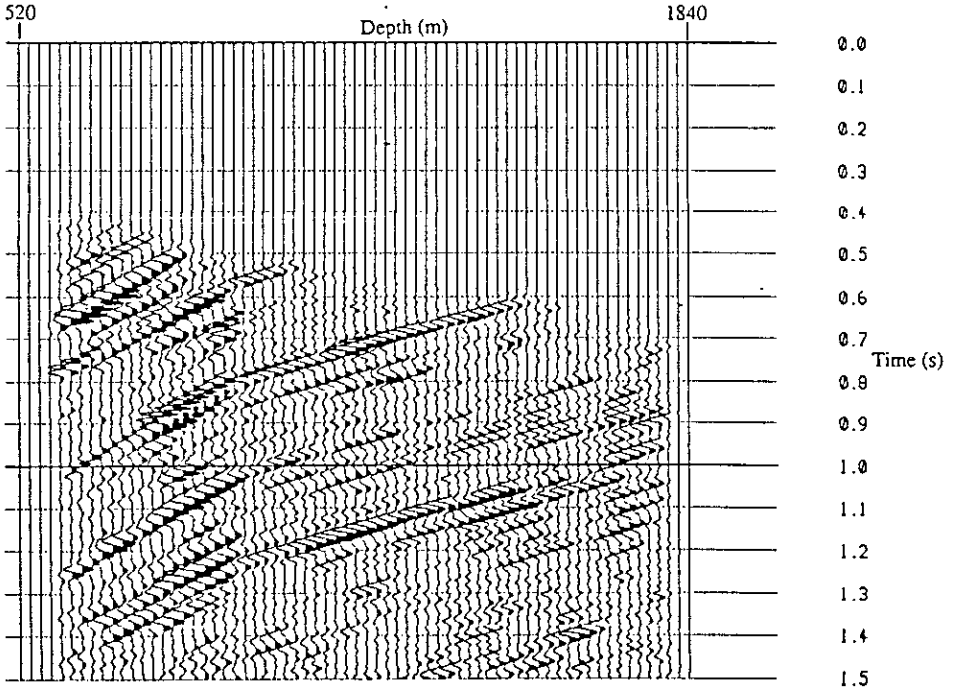

Figure 11. Pass S wavefield for the Rolling Hills data set.

Subsurface mapping of VSP data

When the seismic source used in VSP is offset a certain distance from the borehole, the reflected waves received at the geophone originate from reflection points which are laterally offset from the borehole (Dillon et al.,1984). In this paper, a method of mapping the P-P and P-SV reflections is derived for a flat layered medium with different source and receiver elevations. The method is applied to the P and SV wavefields of the synthetic and field data cases. The separated waves are used in the mapping process.

The method used for mapping P-P reflected waves from an offset VSP was derived by Wyatt and Wyatt (1984) and extended for P-SV waves by Stewart and Labonté (1989).

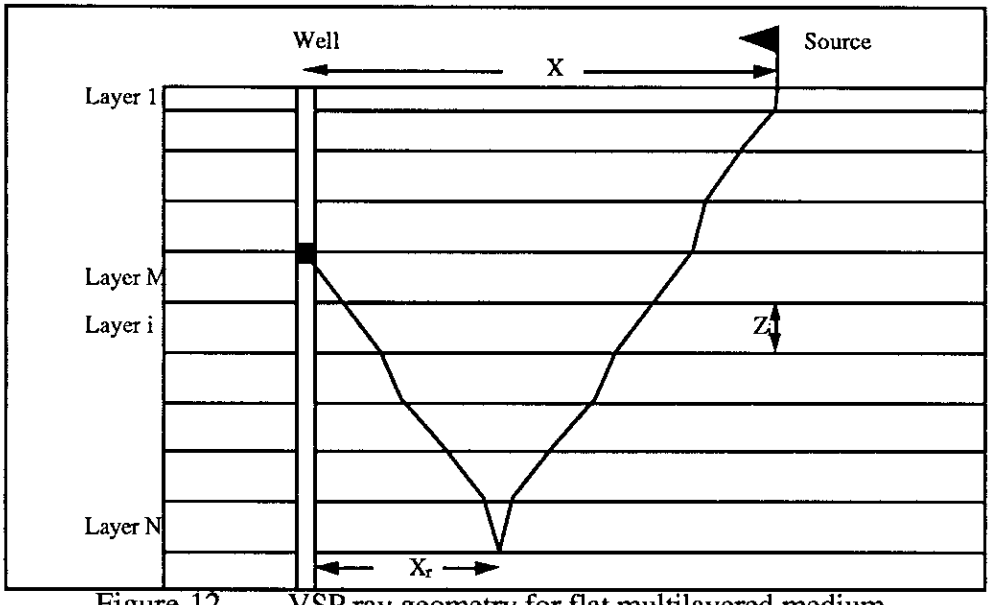

Figure 12. VSP ray geometry for flat multilayered medium.

Figure 12 depicts the VSP ray geometry for a flat multilayered medium. For the P-wave case, the offset distance of the reflection point at layer N, X_r, and the time associated with a reflection from layer N received at layer M, t, are

$$X_r = \frac{X\left[\sum_{i=N}^{M} Z_i \alpha_i\right]}{\left[\sum_{i=N}^{M} Z_i \alpha_i + \sum_{i=1}^{N} Z_i \alpha_i\right]} \tag{4}$$

and

$$t = \sum_{i=1}^{N} \frac{Z_i}{\alpha_i} + \sum_{i=N}^{M} \frac{Z_i}{\alpha_i} + \frac{X^2}{2\left[\sum_{i=1}^{N} Z_i \alpha_i + \sum_{i=N}^{M} Z_i \alpha_i\right]}, \tag{5}$$

and for the P-SV case the results are

$$X_r = \frac{X\left[\sum_{i=N}^{M} Z_i \beta_i\right]}{\left[\sum_{i=N}^{M} Z_i \beta_i + \sum_{i=1}^{N} Z_i \alpha_i\right]} \tag{6}$$

and

$$t = \sum_{i=1}^{N} \frac{Z_i}{\alpha_i} + \sum_{i=N}^{M} \frac{Z_i}{\beta_i} + \frac{X^2}{2\left[\sum_{i=1}^{N} Z_i \alpha_i + \sum_{i=N}^{M} Z_i \beta_i\right]}, \tag{7}$$

where α_i and β_i are the P- and S-wave velocities of the i^{th} layer respectively and Z_i is the thickness of the i^{th} layer.

Equations (4)-(7) provide the mapping between the P-P and P-SV converted wave data and an offset section mapped in two-way normal incidence P time. In practice, for a given depth below the depth level of the trace being mapped, equations (5) and (7) are evaluated giving the raw time (t_i) on the VSP traces corresponding to the depth being mapped. The amplitude of the seismic wavefield at t_i is then mapped to a two-way normal incidence P time for the depth being mapped, and an offset position X_r as evaluated by equations (4) and (6). Bin widths associated with a Common Reflection Point (CRP) for the P-P wave case and a Common Conversion Point (CCP) for the P-SV case case have to be specified so that each mapped point can be placed into its appropriate CRP and CCP bin.

The results for the synthetic data case are shown in Figure 13 for the P-P wave case and Figure 14 for the P-SV wave case while the results for the field data case are shown in Figure 15 for the P-P wave case and Figure 16 for the P-SV wave case. Comparing the exact results obtained from the ray tracer with the mapped results from the synthetic data indicates that the above algorithms map the P or SV reflections within 7% of their correct offset locations and within 4% of their correct time positions.

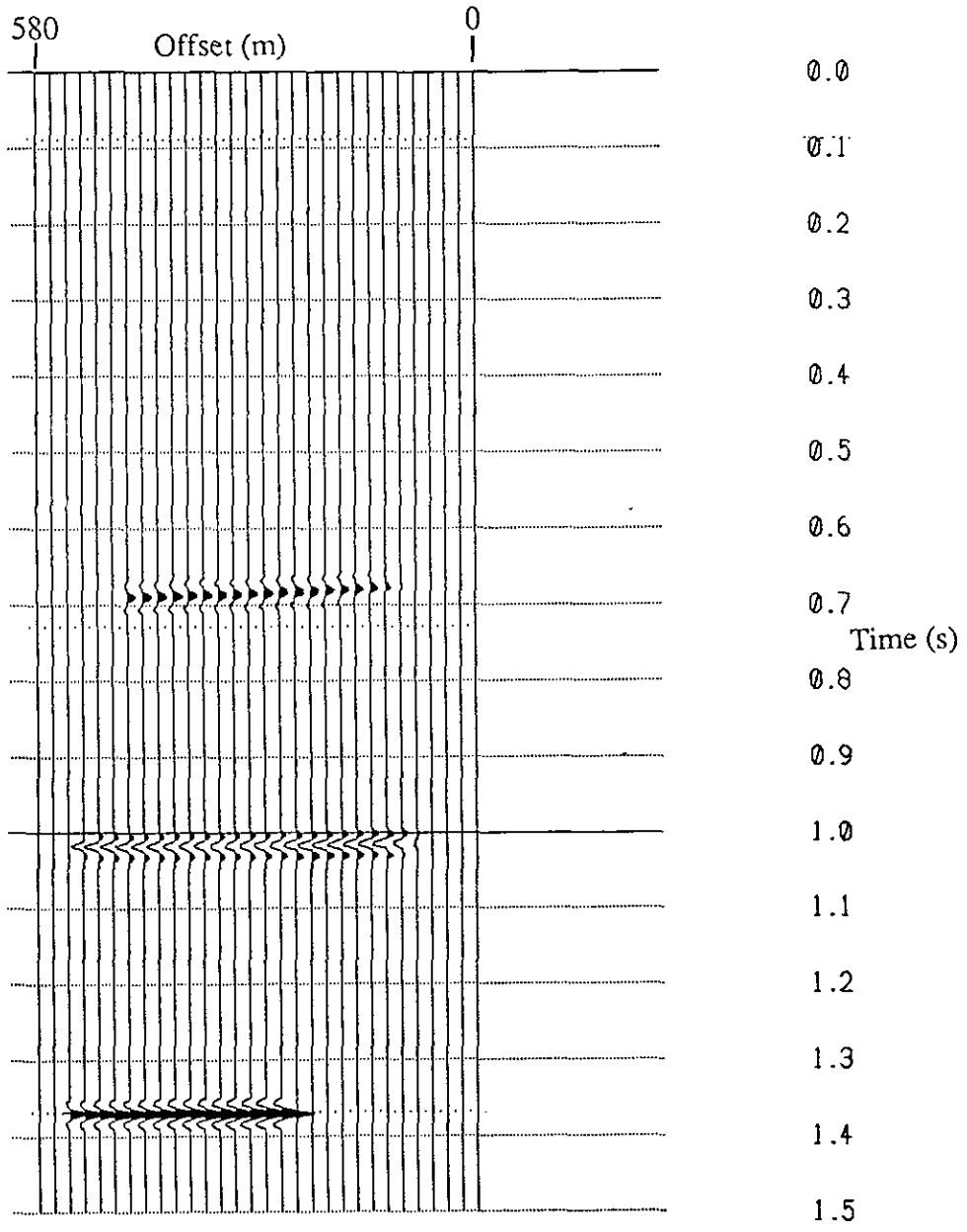

Figure 13. P-wave CRP map for the synthetic data.

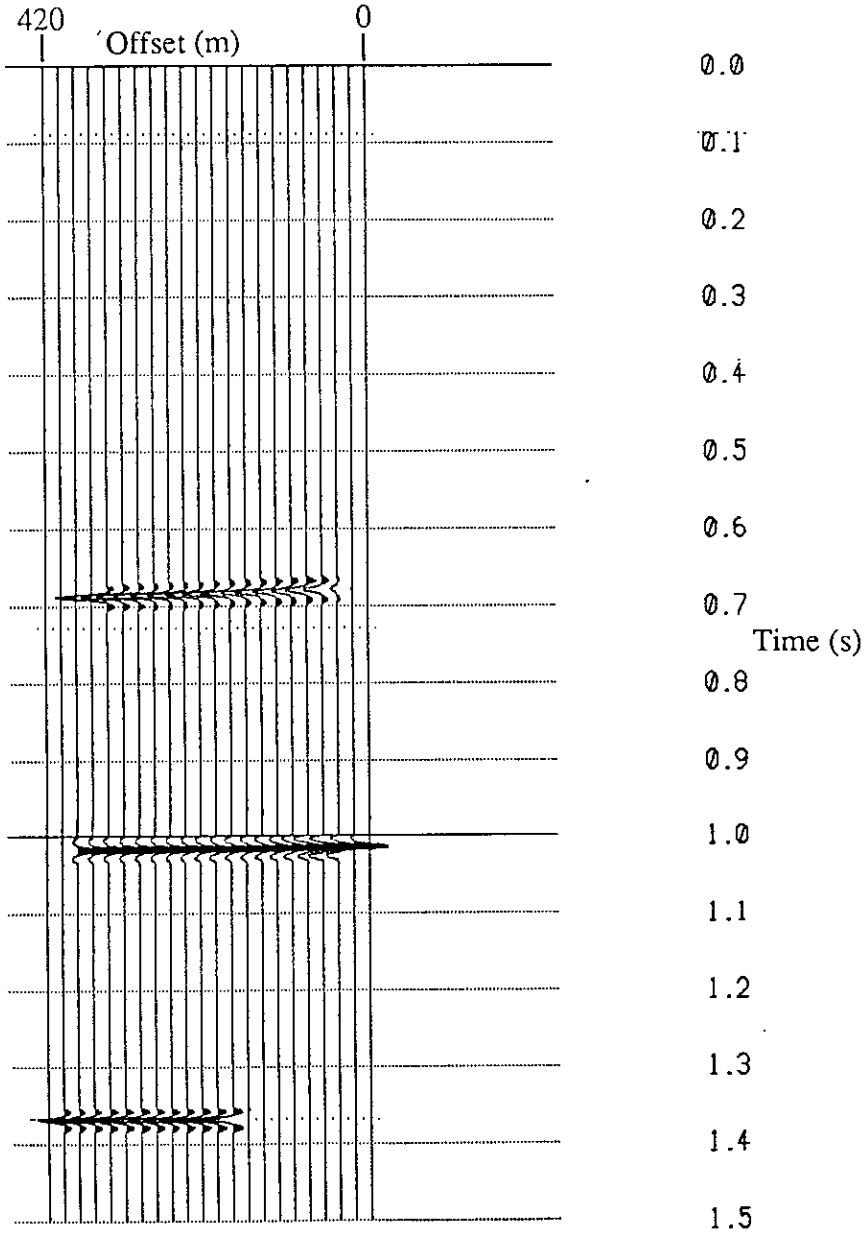

Figure 14. Converted SV-wave CCP map for the synthetic data.

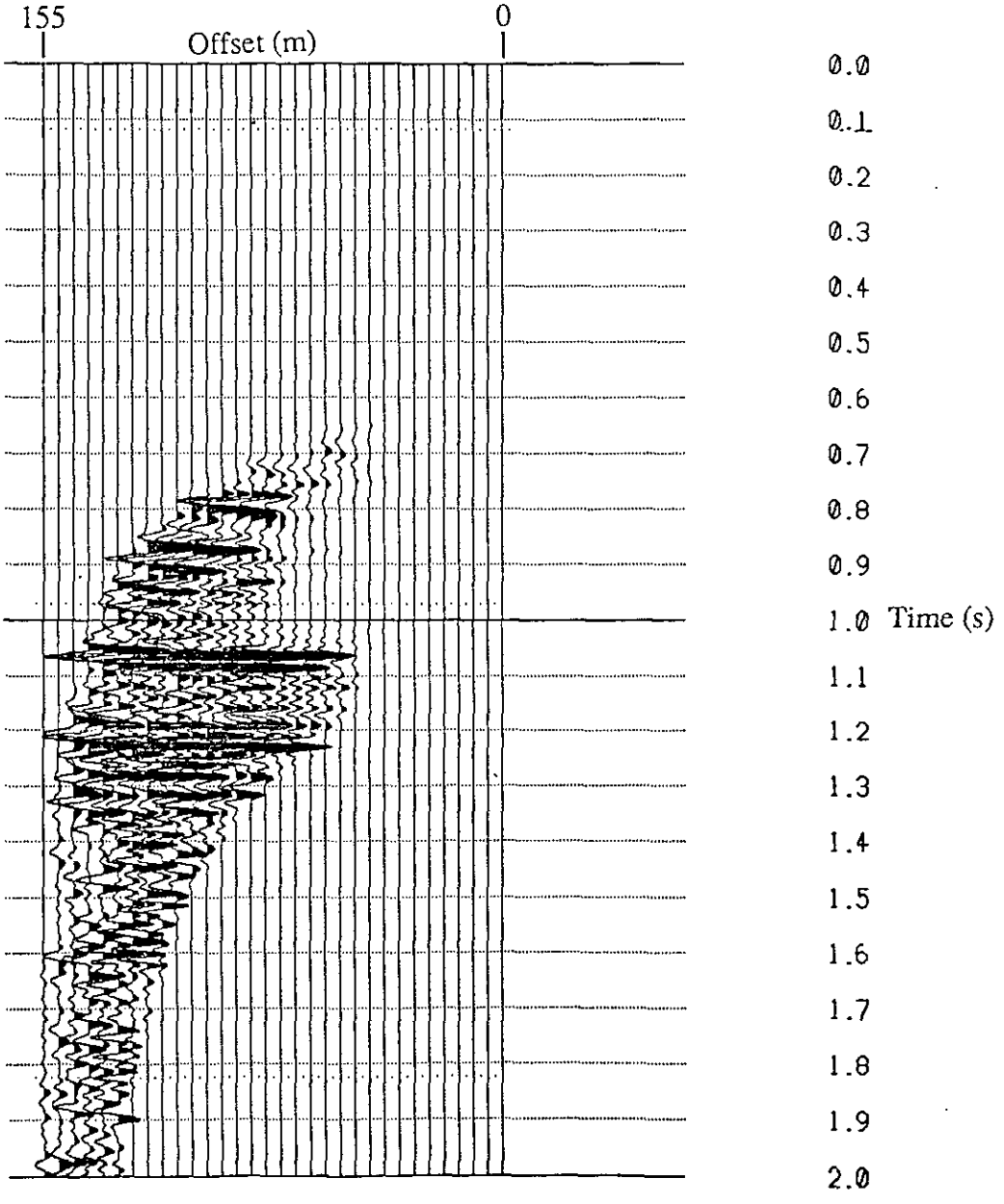

Figure 15. P-wave CRP map for the Rolling Hills data.

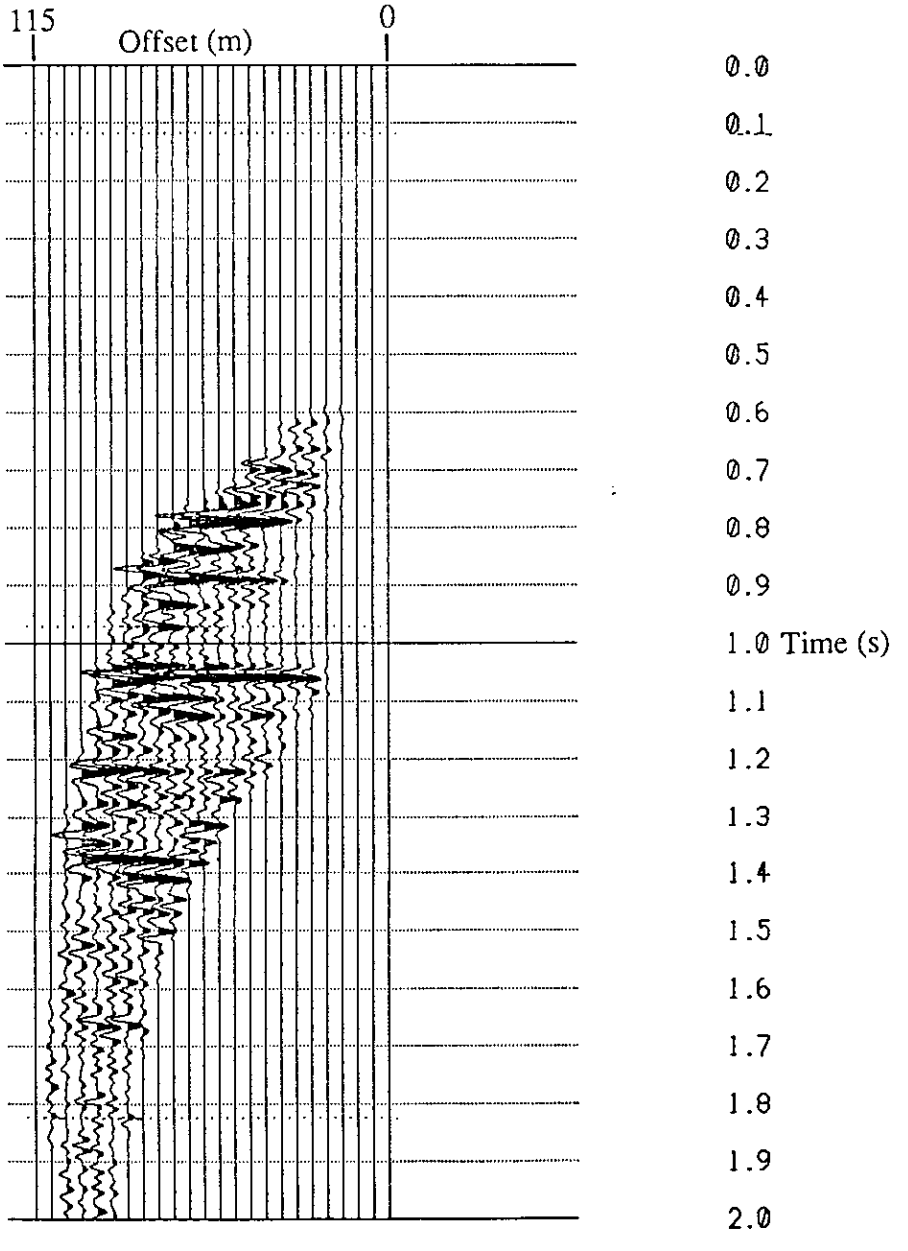

Figure 16. Converted SV-wave CCP map for the Rolling Hills data.

Reflectivity inversion of P-SV converted waves

Mapping the converted wave data provides a section which can be interpreted in structural and perhaps in stratigraphic terms. However, if the actual rock properties are to be analyzed, such as density and velocity, then the inverse problem must be considered. The inverse problem for this case may be stated as: given the converted wave reflectivity, find the shear wave velocity.

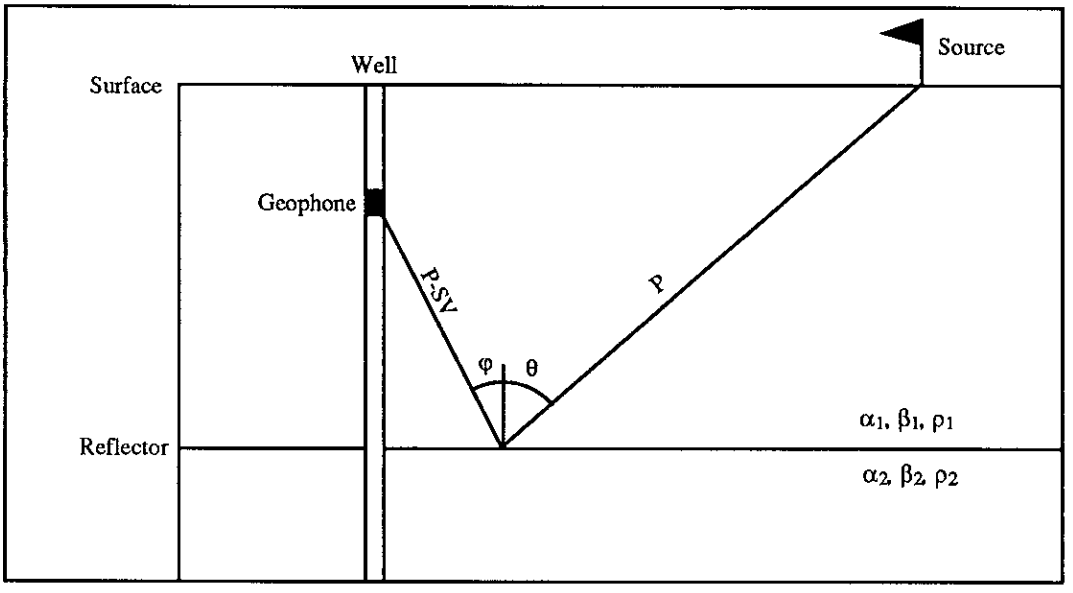

Figure 17. Converted wave reflectivity geometry.

This problem was first approached by Stewart and Labonté (1989) by starting with the expression defining the converted wave (P-SV) reflection coefficient for two half spaces with only small differences in rock properties. With geometry as shown in Figure 17, Aki and Richards (1980) write the displacement reflection coefficient R as

$$R \equiv PS = \frac{-p\alpha}{2\cos\varphi}\left[\left(1-2\beta^2 p^2 + 2\beta^2 \frac{\cos\theta}{\alpha}\frac{\cos\varphi}{\beta}\right)\frac{\Delta\rho}{\rho} - \left(4\beta^2 p^2 - 4\beta^2 \frac{\cos\theta}{\alpha}\frac{\cos\varphi}{\beta}\right)\frac{\Delta\beta}{\beta}\right], \tag{8}$$

where $p = \frac{\sin\theta_1}{\alpha_1}$,

$$\alpha = \frac{\alpha_1 + \alpha_2}{2},\ \Delta\alpha = \alpha_2 - \alpha_1,$$

$$\beta = \frac{\beta_1 + \beta_2}{2},\ \Delta\beta = \beta_2 - \beta_1,$$

$$\rho = \frac{\rho_1 + \rho_2}{2}, \Delta\rho = \rho_2 - \rho_1.$$

Also, to first order $\frac{\sin\theta_1}{\alpha_1} = \frac{\sin\theta}{\alpha} = \frac{\sin\varphi}{\beta}$, and letting $\gamma = \beta/\alpha$ then

$$R = -\frac{\tan\varphi}{2\gamma}\left[\left(1 - 2\gamma^2\sin^2\theta + 2\gamma\cos\theta\cos\varphi\right)\frac{\Delta\rho}{\rho} - \left(4\gamma^2\sin^2\theta - 4\gamma\cos\theta\cos\varphi\right)\frac{\Delta\beta}{\beta}\right], \quad (9)$$

It can be shown (Stewart and Labonté, 1989) that equation (9) can be reduced to

$$\beta_{i+1} = \beta_i \exp\left(-\frac{R^i}{2\sin\varphi_i\left(\cos\theta_i - \tan\varphi_i\right)}\right). \quad (10)$$

In practice, an average of the reflection and incidence angles must be obtained in order to carry out equation (10). This is done by evaluating equation (6) for each time point at every depth level in the pass S VSP section and using X_r and the depth of the reflector being mapped to come up with θ_i and φ_i. These angles are averaged at each time point within every bin location.

This inversion was performed on the P-SV map of the synthetic data for the seven traces belonging to the 240 to 360 m offset range. A value of $\beta_1 = 2500$ m/s was used, and the results are shown in figure 18. The actual values of the S-wave velocities obtained through the inversion is within 1% of the true S-wave velocities used in the model; at least this is true in the regions away from the interfaces where the seismic wavelet introduces artefacts that will be discussed shortly.

The inversion was also performed on the Rolling Hills P-SV map. However, as with most recursion inversion scheme that operate on real data, a low frequency velocity constraint is needed for the final inversion (Lindseth, 1979). This is found from the first break traveltime inversion. The integrated S-wave velocities shown in Figure 19(a) was bandpass filtered using a 0/0 - 10/15 Hz filter to give the low frequency background velocity needed in the inversion (Figure 19(b)). Nine traces, belonging to the 45 to 90 m offset range of the P-SV map of the Rolling Hills data, were inverted as in equation (10) with $\beta_1 = 1200$ m/s as shown in Figure 19(c). These inverted traces were then bandpassed with a 10/15 - 60/75 Hz filter, then added to the low frequency background velocity in Figure 19(b) to yield the final inverted traces shown in Figure 19(d).

The top of the Wabamun (an increase in S velocity) and the top of the Beaverhill Lake salt (a decrease in S velocity) are used to analyze the inversion results. The top of the Wabamun is seen on Figure 19(a) as the large velocity increase at approximately 0.77 s and on Figure 19(c)-(d) as a peak shifted to about 0.8 s. The time shift in the data may be caused by defferent datum points or residual wavelet effects. This wavelet effect is the part

of the reason for the oscillatory signature of the top of the Wabamun. This is observed to occur over a time range equal to the period T of the wavelet, namely T = 0.05 s for this case. The same phenomenon can be observed for the top of the Beaverhill Lake salt which is seen at approximately 1.025 s in Figure 19(a). This same event is again shifted in time on Figures 18(c)-(d) to 1.055 s. The wavelength of the wavelet in this case is shorter than in the Wabamun case, namely T = 0.03 s. The wavelet effect is also present in the synthetic dat as no deconvolution was performed on the synthetic data set. The wavelength of the wavelet in the synthetic data case is of the order of T = 0.02 s.

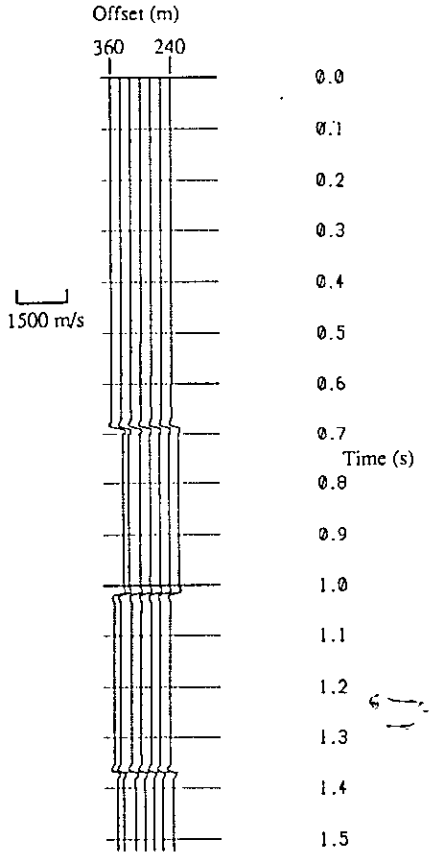

Figure 18. Traces belonging to the 240 to 360 m range of the P-SV map of the synthetic data of Figure 14 inverted using equation (10).

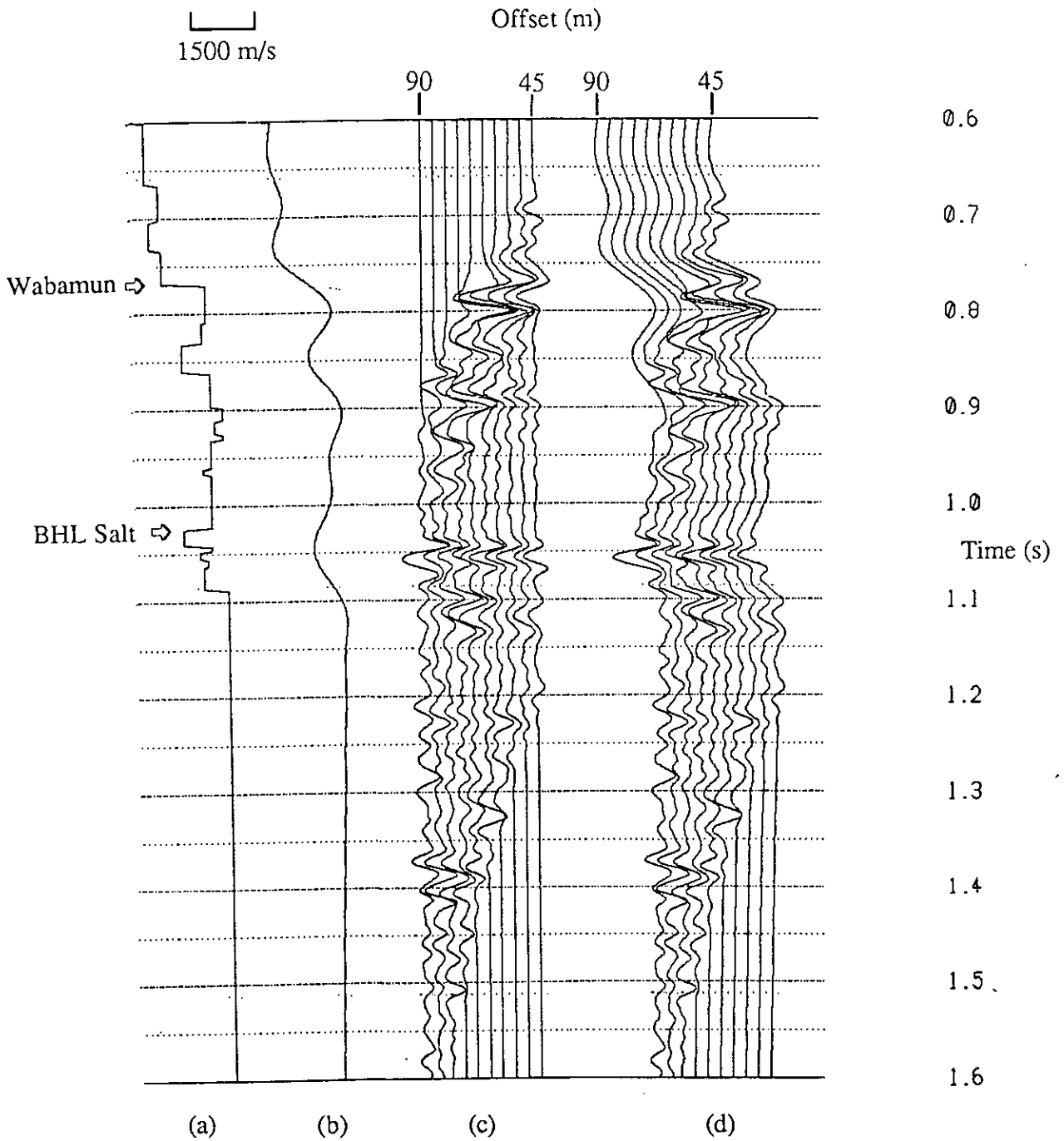

Figure 19. (a) Integrated S-wave velocity from Geis et al. (1989). (b) 0/0 - 10/15 Hz bandpassed version of (a). (c) 45 to 90 m offset traces from the P-SV map of Figure 16 inverted using equation (10). (d) Final inverted traces obtained by adding (b) with a 10/15 - 60/75 Hz bandpassed version of (c). The top of the Wabamun and the top of the Beaverhill Lake (BHL) Salt formations are annotated on the left.

Conclusions

The paper has discussed the processing of synthetic and field multi-component VSP data. The randomly oriented horizontal components of the field VSP are rotated so that one of the two is always oriented toward the source (radial component) and the other is always oriented perpendicular to the source-receiver line (transverse component). The radial and vertical components are then used to equalize the energy present on both components in a time window centered on the first breaks. This is done as a first step in amplitude recovery and also to assure that there will not be any strong amplitude variations between adjacent traces in the VSP sections caused by coupling variations of the geophone between depth levels or by source amplitude variations between shots. The downgoing wavefield is then removed to yield to the more important upgoing wavefield. This is done by enhancing the downgoing wavefield using the p - t decomposition, in which the whole wavefield is transformed into the slowness domain and only the positive slownesses are used in the reconstruction. The enhanced wavefield is then subtracted from the total wavefield to yield the upgoing wavefield. This is done on both the radial and vertical components. For the synthetic case, the downgoing wavefield is removed by muting the first breaks. A velocity inversion is then performed on the data using the first downgoing P and S arrivals to give a P- and S-wave interval velocity function that will later be used for separating and mapping the P and S waves and inverting the S-wave map. A spiking deconvolution is performed on the field VSP. The filters are designed on a time series obtained by the vector addition of the first P breaks on the vertical and radial components of the enhanced downgoing wavefield for each trace. These filters are then applied to the vertical and radial components of the upgoing wavefield. The second step in amplitude recovery is then taken by applying a time-variant exponential gain to the data. The same gain is applied to the vertical and radial components so that polarization angle information is not lost.

The P-S wave mode separation is performed on the vertical and radial components of the deconvolved, gained upgoing wavefield. The filter coefficients are derived by considering the displacement of incident P and S waves at the geophone location. Instabilities at slownesses $|p| > 1/V_S$ are eliminated by tapering the coefficients to zero at these slownesses. The separation is performed on the synthetic and field data in the p - t and f - k domains. The ringing and smearing of energy is noticeable on the results obtained through the f - k domain for both the synthetic and real data cases. The results obtained through the p - t decomposition method have less smearing or ringing.

The mapping of the P-P and P-SV reflections is performed on the pass P and pass S sections for the synthetic and field cases from the P-S wave mode separation results obtained through the p - t decomposition method. Both the P-P and P-SV reflections are mapped to a two way normal incidence P-wave time. The errors in the mapping, caused amongst other things by small angle approximations in the derivation of the mapping algorithm, are assessed by inspection of the synthetic maps. The maximum error in offset mapping reaches 7% of the true offset location when the angle of incidence is 60° and the maximum error in time mapping is 4% of the true time location of the event.

The S-wave velocity inversion gives results that within 1% of the true S-wave velocity for the synthetic case. However, in the field case, the inversion is strongly affected by the deconvolution used on the data. If the deconvolution would perform perfectly so that the events are spiked, the inversion would perform much better. The wave character of the input data leaves an undesirable artefact in the resulting velocity. This so called wavelet effect is observed on both the synthetic and field data cases.

References

Aki, K. and Richards, P. G., 1980, Quantitative seismology: Theory and methods, v. 1: W. H. Freeman and Co.

Cheadle, S. P., 1988, Applications of physical modeling and localized slant stacking to a seismic study of subsea permafrost: Ph.D. Thesis, The University of Calgary, Calgary, Alberta, Canada.

Dankbaar, J. W. M., 1987, Vertical seismic profiling - Separation of P- and S-waves: Geophys. Prosp., 35, 803-814.

Dillon, P. B. and Thompson, R. C., 1984, Offset source VSP surveys and their image reconstruction: Geophys. Prosp., 32, 5, 790-811.

Foster, D. J. and Gaiser, J. E., 1986, Elastic wave field decomposition of offset VSP data: Soc. of Expl. Geophys. Ann. Mtg, Expanded Abstracts, 563-565.

Geis, W. T., Stewart, R. R., Jones, M. and Katapodis, P., 1989, An integrated P-SV study: Rolling Hills, Southern Alberta: submitted to Geophysics.

Lindseth, R. O., 1979, Synthetic sonic logs - A process for stratigraphic interpretation: Geophys., 44, 1, 3-26.

Stewart, R. R. and Labonté, S., 1989, VSPCCP map and AVO inversion for P-SV waves: in preparation.

Wyatt, K. D. and Wyatt, S. B., 1984, Determining subsurface structure using the vertical seismic profile, in Toksoz, M. N. and Stewart, R. R., Eds., Vertical seismic profiling, Part B: Advanced concepts: Geophysical Press.